Capturing Soil Surface Freeze Dynamics Over the Arctic-Boreal Zone With GNSS-Reflectometry

Hugo Carreno-Luengo, *Senior Member, IEEE*, Christopher S. Ruf, *Life Fellow, IEEE*, Scott Gleason, *Senior Member, IEEE*, and Anthony Russel

***Abstract*— The Arctic-boreal zone (ABZ) is warming due to climate change. Current spaceborne remote sensing techniques and retrieval methodologies need to be complemented to improve systematic monitoring of the cryosphere. To that end, this article presents a new investigation of the use of the global navigation satellite system reflectometry (GNSS-R) remote sensing technique by a SmallSat constellation. A new freeze/thaw (F/T) seasonal multithresholding algorithm (STA) is developed using high-inclination orbit near-Nadir Spire Global GNSS-R data acquired through the National Aeronautics and Space Administration (NASA) Commercial Smallsat Data Acquisition (CSDA) Program. Five different soil surface reflectivity Γ models are proposed to account for the impact of vegetation cover and small-scale surface roughness on Earth-reflected GNSS signals. The sensitivity of the Γ models to F/T surface state transitions is evaluated, and the optimum model is selected to construct a seasonal scale factor. Then, a multithresholding matrix is obtained for F/T classification using a specific threshold for every surface grid cell. Results for the annual frozen soil duration (days yr^{-1}) are compared with those by the Soil Moisture Active Passive (SMAP) mission. Additionally, freezing and thawing periods are analyzed to determine when the moisture exchange with the atmosphere is locked, which is an important climatic factor. A novel metric is introduced to characterize the freeze intensity moving beyond classical F/T binary classifications. Results are evaluated using air and soil temperature, snow depth and temperature, and soil moisture content (SMC) provided by the European Centre for Medium-Range Weather Forecasts (ECMWF) ERA5-Land reanalysis product.**

***Index Terms*— Arctic-boreal zone (ABZ), freeze/thaw (F/T), global navigation satellite system reflectometry (GNSS-R), monitoring, NASA Commercial Smallsat Data Acquisition (CSDA), Spire Global.**

I. Introduction

THE Arctic-boreal zone (ABZ) includes the boreal, sub-Arctic, and Arctic climate zones. ABZ surface temperature is warming faster than the overall Earth's surface [1], [2]. Indeed, since the 1980s, the rate of warming has been three times higher than the global average. This is known as polar amplification [3]. Surface temperature is one of the most important observations required for ABZ monitoring because it is a key parameter that rules physical and radiative properties of the Earth's surface. One specific ABZ element affected by this phenomenon is the cryosphere, including the surface freeze/thaw (F/T) cycle, which is the focus of this investigation. This topic is of high relevance because the warming ABZ is reducing the duration of freezing periods and degrading permafrost.

Remote sensing monitoring of the F/T cycle over the ABZ is challenging because of the common presence of clouds, the annual period of darkness at high latitudes, and the presence of snow and vegetation, e.g., boreal forests, over the Earth's surface. L-band passive microwave radiometry data by instruments aboard low Earth orbit (LEO) missions, e.g., European Space Agency (ESA) Soil Moisture Ocean Salinity (SMOS) [4] and National Aeronautics and Space Administration (NASA) Soil Moisture Active Passive (SMAP) [5] have been used for determining landscape F/T state with ∼40-km spatial resolution and ∼3 days temporal resolution. On the other hand, LEO-based synthetic aperture radar (SAR) missions provide improved spatial resolution ∼100 m, but lower temporal resolution ∼7–14 days. C-band, e.g., ESA Sentinel-1 [6], [7], and L-band, e.g., Advanced Land Observation Satellite (ALOS) [7], [8] SAR data, have been used for F/T detection. However, the F/T surface state is highly variable with time and surface location, and improved spatiotemporal monitoring capabilities are required to capture the large F/T heterogeneity, especially in the ABZ.

Global navigation satellite system reflectometry (GNSS-R), which is a type of L-band passive multibistatic radar, e.g., Martín-Neira [9], Ruf et al. [10], and Unwin et al. [11], provides an alternative approach for F/T spaceborne remote sensing monitoring from LEO. Recent studies with SMAP GNSS-R mode [12], TechDemoSat-1 [13], [14], and NASA CYclone Global Navigation Satellite System (CYGNSS) [15], [16] demonstrated this capability over high-latitude and high-altitude terrains. GNSS-R instruments can be operated by SmallSats because of the low power consumption and the relatively low antenna gain required for generating high-quality scientific data, and because of the use of the GNSS constellations, e.g., USA Global Positioning System (GPS), as radar transmitters. On the other hand, the number of GNSS-R missions, including constellations,

Received 9 October 2024; revised 27 February 2025 and 2 April 2025; accepted 10 May 2025. Date of publication 14 May 2025; date of current version 9 July 2025. This research was supported in part by the NASA Research Opportunities in Space and Earth Science (ROSES) award 80NSSC24K1499 and in part by the NASA Science Mission Directorate contract 80LARC21DA003 with the University of Michigan. *(Corresponding author: Hugo Carreno-Luengo.)*

Hugo Carreno-Luengo, Christopher S. Ruf, and Anthony Russel are with the Department of Climate and Space Sciences and Engineering, University of Michigan, Ann Arbor, MI 48109 USA (e-mail: carreno@umich.edu; cruf@umich.edu; russelan@umich.edu).

Scott Gleason is with Daaxa LLC, Boulder, CO 80307 USA (e-mail: sgleason@protonmail.com).

Digital Object Identifier 10.1109/TGRS.2025.3570213

© 2025 The Authors. This work is licensed under a Creative Commons Attribution 4.0 License.
For more information, see https://creativecommons.org/licenses/by/4.0/

is expected to keep increasing in the near future. Examples of current operational GNSS-R SmallSats missions are NASA CYGNSS [17], TAiwan Space Agency (TASA) TRITON [18], BuFeng-1 A/B [19], FengYun-3 [20], ESA Passive REflectometry and dosimeTrY (PRETTY) [21], and upcoming ESA HydroGNSS [11]. Additionally, operational commercial constellations, e.g., Spire Global [22], Muon Space [23], and Tianmu-1 [24], are also contributing to the scientific community.

F/T surface changes lead to changes in the surface permittivity [25], [26], [27]. The permittivity increases when the surface temperature moves from below 0 °C to above 0 °C. The foundation of F/T retrieval by GNSS-R is based on how these changes affect surface reflectivity Γ. Liquid water in thawed soils increases the permittivity compared to frozen terrain, increasing the reflectivity Γ. The main goal of this investigation is to further develop F/T detection and monitoring capabilities over the ABZ using high-inclination orbit GNSS-R SmallSat constellations. Spire Global near-Nadir GNSS-R data [22], [28] acquired through the NASA Commercial Smallsat Data Acquisition (CSDA) Program [29] are used in this investigation. The methodology presented here is aimed to be applicable also by different constellations of commercial GNSS-R SmallSats, e.g., Muon Space [23], and by the ESA Scout HydroGNSS mission [11]. F/T timing is an important observable, which determines the moisture exchange. This measurement remains challenging in the ABZ because of the variety of land cover types, the presence of thick snow cover, and moderate-to-heavy vegetation cover, e.g., boreal forests. GNSS-R L-band measurements have the intrinsic ability to penetrate clouds and partially biomass, with an excellent sensitivity to changes in soil surface permittivity when water changes its state from liquid to solid. GNSS-R measurements depend only slightly on the physical temperature of the Earth's surface, while passive microwave radiometers, e.g., SMAP and SMOS, depend more strongly. On the other hand, the scattering over land surface is quite specular, and thus, the spatial resolution is higher than microwave radiometry.

This article is organized as follows. First, we introduce the core and auxiliary data products in Section II. Then, the methodology is presented in Section III, describing the semi-empirical modeling and its optimization, as well as the multithresholding algorithm used for F/T classification. Then, the results are presented and evaluated in Section IV, including the annual frozen soil duration (days yr^{-1}) and a comparison with the SMAP F/T radiometer product, the novel freeze intensity (FI) observable, and an analysis of freezing and thawing periods. Finally, Section V concludes this article.

II. Data Products

A. NASA CSDA Spire Global GNSS-R Data

The Spire near-Nadir GNSS-R Level 1 data product [22] is selected for this study over the ABZ. The Spire near-Nadir constellation is composed of five operational LEO CubeSats distributed in batch-1 (2 CubeSats, 1 decommissioned, ∼35° inclination, ∼564-km altitude of perigee, and peak science antenna gain ∼9.5 dBi), batch-2 (2 CubeSats, ∼97° inclination, ∼520-km altitude of perigee, and peak science antenna gain ∼8.5 dBi), and batch-3 (1 CubeSat, ∼97° inclination, ∼474 km altitude of perigee, and peak science antenna gain ∼8.5 dBi). This multiconstellation dataset is generated with GPS L1 C/A, Galileo E1 CA, Beidou B1 C_pilot, and QZSS L1 CA signals collected at the left-hand circular polarization (LHCP). Spire uses the classical GNSS-R technique to obtain the delay Doppler maps (DDMs), which are the foundational observables from which the point reflectivity Γ is derived. The reflected signal is correlated coherently with a local replica of the transmitted signal after adjusting the Doppler frequency shift. Reflected signals are dynamically calibrated using direct GNSS signals' power measurements by an onboard receiver. Several quality filters are applied, and data are selected for incidence angles lower than $\theta_i < 70°$ and reflectivity 40 dB $< \Gamma <$ 0 dB. Data out of these limits are considered of low quality and not included in the processing chain.

B. NASA SMAP Auxiliary Data

The SMAP Enhanced L3 Radiometer Global and Polar Grid Daily 9-km EASE-Grid Soil Moisture, Version 5 [30] and the SMAP Enhanced L3 Radiometer Global and Northern Hemisphere Daily 9-km EASE-Grid F/T State, Version 3 [31] data products are selected for this study. The following key variables are used as sources of auxiliary information for the development and evaluation of the GNSS-R F/T seasonal multithresholding algorithm (STA).

1) The F/T surface classifier, which is a Boolean variable that indicates whether the soil surface within a grid cell is frozen or thawed.
2) The static water body fraction W_f, which is obtained from the MOD44W database of permanent open fresh water by the Moderate Resolution Imaging Spectroradiometer (MODIS), with auxiliary Shuttle Radar Topography Mission (STRM) digital elevation model (DEM) based topographic information.
3) The vegetation water content (VWC) applied to the current single-channel algorithm (SCA). The SMAP dual-channel algorithm (DCA) directly retrieves vegetation optical depth (VOD) without referring to auxiliary data, along with soil moisture content (SMC), but this is not available over frozen terrain regions during freezing periods. The new SMAP improved SCA-based VWC estimation includes water content contributions from the foliage and stem components, adjusted for land cover type using the MODIS International Geosphere–Biosphere Program (IGBP) classification scheme.
4) The roughness parameter generated by the SMAP DCA h.

C. ECMWF ERA5-Land Auxiliary Data

The European Centre for Medium-Range Weather Forecasts (ECMWF) ERA5-Land reanalysis dataset is used to provide auxiliary data at hourly time scale, at a spatial resolution of

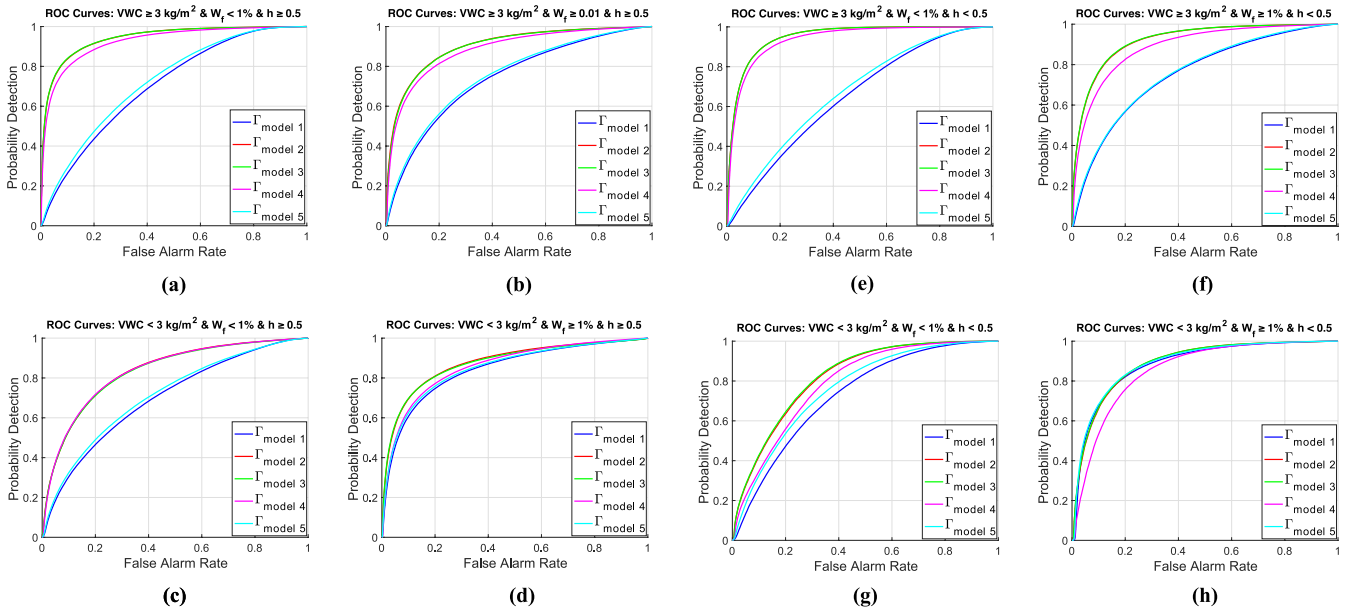


Fig. 1. Sensitivity analysis (full year of data) of the proposed seasonal scale factor models over ABZ using ROC curves over different surface types classified according to VWC, W_f, and h. (a) VWC $\geq$ 3 kg/m^2, $W_f < 0.01$, and $h \geq 0.5$. (b) VWC $\geq$ 3 kg/m^2, $W_f \geq 0.01$, and $h \geq 0.5$. (c) VWC $<$ 3 kg/m^2, $W_f < 0.01$, and $h \geq 0.5$. (d) VWC $<$ 3 kg/m^2, $W_f \geq 0.01$, and $h \geq 0.5$. (e) VWC $\geq$ 3 kg/m^2, $W_f < 0.01$, and $h < 0.5$. (f) VWC $\geq$ 3 kg/m^2, $W_f \geq 0.01$, and $h < 0.5$. (g) VWC $<$ 3 kg/m^2, $W_f < 0.01$, and $h < 0.5$. (h) VWC $<$ 3 kg/m^2, $W_f \geq 0.01$, and $h < 0.5$. Overall, $\Gamma_{\text{model 2}}$ and $\Gamma_{\text{model 3}}$ provide the best performance. $\Gamma_{\text{model 5}}$ improves in low-vegetated areas.

$0.1^\circ \times 0.1^\circ$ [32]. The following key-variables are selected as sources of auxiliary information for the development of the F/T STA algorithm and the interpretation of the results:

1) The air temperature T_{air} (°C) at 2 m above the land surface.
2) The temperature of the soil T_{soil} (°C) in layer 1 (0–7 cm), which is selected because this is approximately the signal penetration depth at the L band.
3) The snow cover fraction (%) of the grid cell.
4) The cell average of the snow depth D_{snow} (m) on the ground, excluding snow on canopy.
5) The melting of snow averaged over the grid cell M_{snow} (m of water equivalent). This variable is accumulated from the beginning to the end of the forecast time step.
6) The temperature of the snow layer from the ground to the snow-air interface T_{snow} (°C).
7) The SMC (m^3/m^3) in soil layer 1 (0–7 cm), which is of relevance for L-band signals.
8) The leaf area index (LAI) for high and low vegetation, which is one-half of the total green leaf area per unit horizontal ground surface area for high or low vegetation type.

III. Methodology: F/T STA

This section describes the F/T STA algorithm. First, the seasonal scale factor $\Delta(t)$ is defined and optimized. Then, a multithresholding method is described and applied to $\Delta(t)$. This semi-empirical retrieval algorithm is used to generate the soil surface F/T classification.

A. F/T Seasonal Scale Factor: Soil Surface Reflectivity Modeling

The foundational observable of the F/T STA algorithm is based on the relationship between time t series of soil surface reflectivity $\Gamma(t)$ and seasonal reference frozen Γ_{freeze} and thawed Γ_{thaw} surface states at every grid cell. For a measurement at time t, the seasonal scale factor $\Delta(t)$ is defined as follows [15], [16]:

$$\Delta(t) = \frac{\Gamma(t) - \Gamma_{\text{freeze}}}{\Gamma_{\text{thaw}} - \Gamma_{\text{freeze}}}. \tag{1}$$

The frozen and thawed references states are calculated as the 5% and the 95% points in the cumulative distribution function (cdf) of Γ at each pixel, during Winter (Γ_{freeze}) and Summer (Γ_{thaw}). Different F/T surface states are related to the associated time period of analysis. Originally, this algorithm was developed for studies over homogeneous regional target areas with low vegetation at lower latitudes, e.g., Tibet Plateau, Andes Mountains, and Rocky Mountains [15], [16]. Consequently, the surface reflectivity $\Gamma_{\text{model 1}}$ was modeled by [33], [34]

$$\Gamma_{\text{model 1}} = \frac{(4\pi)^2 \left(Y_p - Y_n\right)(U_r + U_t)^2}{\lambda^2 G_r \text{EIRP}} \tag{2}$$

where Y_p is the peak value of the power DDMs and Y_n is the noise floor, which is calculated from the power DDMs. U_r is the distance between each Spire spacecraft and the nominal specular points, U_t is the distance between each GNSS satellite and the nominal specular points, λ is the signal wavelength, G_r is the receiver antenna gain, and EIRP is the equivalent isotropically radiated power.

The goal of the present investigation is to generate global-scale F/T retrievals over the ABZ, which is characterized by highly heterogeneous land cover types. To do so, several additional surface reflectivity Γ models are proposed and evaluated to address the more complicated land surfaces being considered. In the second model $\Gamma_{\text{model 2}}$, the VOD is parameterized as $\tau = \alpha \text{LAI}$, where α is an empirical adjusting factor. The selected default factor is $\alpha = 2$, which

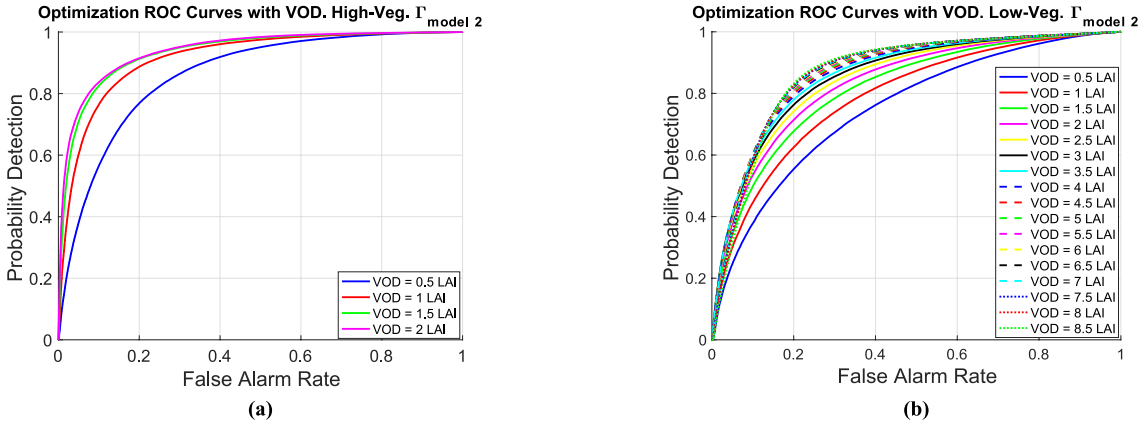


Fig. 2. Empirical optimization of ROC curves by adjusting the VOD parametrization in $\Gamma_{\text{model 2}}$, i.e., tuning the α parameter in $\tau = \alpha \text{LAI}$. (a) High vegetation surface type [VWC $\geq$ 3 kg/m^2, $W_f < 0.01$, and $h \geq 0.5$]. (b) Low vegetation surface type [VWC $<$ 3 kg/m^2, $W_f < 0.01$, and $h \geq 0.5$]. A similar optimization approach is used for all the surface types: $\alpha_{\text{opt}} = 2$ for [VWC $\geq$ 3 kg/m^2, $W_f < 0.01$, and $h \geq 0.5$]. $\alpha_{\text{opt}} = 3$ for [VWC $\geq$ 3 kg/m^2, $W_f \geq 0.01$, and $h \geq 0.5$]. $\alpha_{\text{opt}} = 8.5$ for [VWC $<$ 3 kg/m^2, $W_f < 0.01$, and $h \geq 0.5$]. $\alpha_{\text{opt}} = 4$ for [VWC $<$ 3 kg/m^2, $W_f \geq 0.01$, and $h \geq 0.5$]. $\alpha_{\text{opt}} = 4$ for [VWC $\geq$ 3 kg/m^2, $W_f < 0.01$, and $h < 0.5$]. $\alpha_{\text{opt}} = 2.5$ for [VWC $\geq$ 3 kg/m^2, $W_f \geq 0.01$, and $h < 0.5$]. $\alpha_{\text{opt}} = 3.5$ for [VWC $<$ 3 kg/m^2, $W_f < 0.01$, and $h < 0.5$]. $\alpha_{\text{opt}} = 1$ for [VWC $<$ 3 kg/m^2, $W_f \geq 0.01$, and $h < 0.5$]. Intermediate α values above α_{opt} are not included to improve the clarity of the figures.

accounts for the downwelling and upwelling paths of the GNSS-R signals [35]. This estimation can be used when direct τ retrievals are not possible [36], [37], [38]. τ can also be linearly related to VWC for low vegetated areas. On the other hand, τ correlates well with normalized difference vegetation index (NDVI) and LAI for a wide range of vegetation types, including forest [39]. Scattering effects are assumed to be negligible at the L-band. The main effect of the vegetation layer is to attenuate incident and reflected GNSS-R signals. The transmissivity of the upwelling vegetation $\gamma = e^{-\alpha \text{LAI}}$ is compensated to properly estimate the soil surface reflectivity $\Gamma_{\text{model 2}}$

$$\Gamma_{\text{model 2}} = \frac{(4\pi)^2 \left(Y_p - Y_n\right)(U_r + U_t)^2}{\lambda^2 G_r \text{EIRP}} e^{\alpha \text{LAI}}. \tag{3}$$

The total LAI is calculated using ERA5-Land auxiliary data [40], [41] as the sum of $c_{\text{high}}\text{LAI}_{\text{high}}$ and $c_{\text{low}}\text{LAI}_{\text{low}}$. c represents LAI cover fraction [%], and subscripts high and low denote high and low vegetation types [40, Table 8.1]. ERA5-Land LAI is based on the data product MOD15A2 by MODIS onboard TERRA [42]. LAI is defined as the volumetric integral of the canopy structure [40]. This key variable determines the 3-D radiation field in vegetation canopies, and it is formally defined by various canopy radiation models [42].

The next Γ model, $\Gamma_{\text{model 3}}$, builds on $\Gamma_{\text{model 2}}$ by additionally incorporating the correction of the effective small-scale surface roughness by adding the roughness parameter h and the impact of the incidence angle θ_i. Theoretically, under the Kirchhoff model with a physical optics approximation, this effect is modeled by the factor $e^{-(2k\sigma \cos\theta_i)^2}$, where k is the signal angular wavenumber and σ is the surface height standard deviation, which is related to small-scale surface roughness. The roughness parameter h is an estimation of the factor $h \sim (2k\sigma)^2$, and the angular correction accounts for the effective surface roughness [30]. Considering these elements, the reflectivity $\Gamma_{\text{model 3}}$ can be estimated as follows:

$$\Gamma_{\text{model 3}} = \frac{(4\pi)^2 \left(Y_p - Y_n\right)(U_r + U_t)^2}{\lambda^2 G_r \text{EIRP}} e^{\alpha \text{LAI}} e^{h(\cos\theta_i)^2}. \tag{4}$$

As a further correction, the angular dependence of the signal propagation path through the vegetation cover is included in a fourth model to account for the larger signal path at higher incidence angles θ_i, which increases the attenuation of incident and scattered signals. The resulting reflectivity $\Gamma_{\text{model 4}}$ is given by

$$\Gamma_{\text{model 4}} = \frac{(4\pi)^2 \left(Y_p - Y_n\right)(U_r + U_t)^2}{\lambda^2 G_r \text{EIRP}} e^{\alpha \text{LAI}/\cos\theta_i} e^{h(\cos\theta_i)^2}. \tag{5}$$

Finally, we propose a different model for VOD, which is estimated as $\tau = 2b\text{VWC}$, where b is an SMAP-derived parameter that accounts for the structural effects of the upwelling vegetation. This τ estimation is used by SMAP in the SCA mode and is incorporated here with an additional factor 2, which accounts for the downwelling and upwelling paths of the GNSS-R signals. The resulting surface reflectivity model $\Gamma_{\text{model 5}}$ is given by

$$\Gamma_{\text{model 5}} = \frac{(4\pi)^2 \left(Y_p - Y_n\right)(U_r + U_t)^2}{\lambda^2 G_r \text{EIRP}} e^{2b\text{VWC}/\cos\theta_i} e^{h(\cos\theta_i)^2}. \tag{6}$$

B. F/T Seasonal Scale Factor: Sensitivity Analysis, Selection, and Optimization

A sensitivity analysis (Fig. 1) is carried out to evaluate the performance of the seasonal scale factor $\Delta(t)$ using the five different proposed Γ models over a variety of surface types classified according to VWC, W_f, and h. The values used for the surface classification (VWC = 3 kg/m^2, $W_f = 0.01$, and $h = 0.5$) have been empirically selected for the GNSS-R scene, considering the quality flags used by an L-band passive microwave radiometry mission, i.e., SMAP. A family of

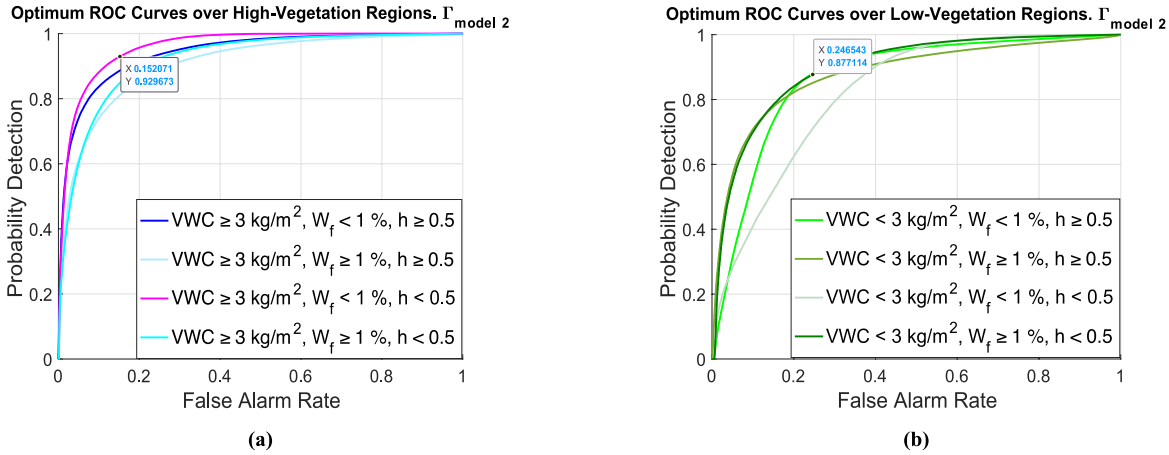


Fig. 3. Optimum ROC curves for all surface types classified in two families: (a) VWC $\geq$ 3 kg/m^2 and (b) VWC $<$ 3 kg/m^2. ROC curves derived with $\Gamma_{\text{model 2}}$. The coordinates of the point of maximum sensitivity [15], [16] of two sample curves are illustrated. Each curve has its own point of maximum sensitivity, not included in this figure to avoid overlapping. The sensitivity is lower in family (b) because these surfaces mainly correspond to arid desert terrain where dry soil permittivity reduces Γ, i.e., because the freezing of the soil water marks the permittivity in a roughly similar way as dry terrain. Overall, the PD versus FAR is excellent, which demonstrates the high sensitivity of the seasonal scale factor $\Delta(t)$ with $\Gamma_{\text{model 2}}$ to F/T transitions.

receiver operating characteristic (ROC) curves [15], [16] is constructed using $\Delta(t)$ and ERA5-Land air temperature T_{air} as proxy reference data (Fig. 1). The true freeze reference state is selected when $T_{\text{air}} < -5$ °C, and the true thaw reference state is selected when $T_{\text{air}} > 5$ °C. These references provide higher confidence on the surface state than references closer to 0 °C, leading to an improved sensitivity of $\Delta(t)$ to F/T transitions. Overall, $\Gamma_{\text{model 2–4}}$ provide a better probability of detection (PD) versus false alarm rate (FAR) performance according to the ROC curves than $\Gamma_{\text{model 1}}$, which neglects vegetation effects, and $\Gamma_{\text{model 5}}$, which uses $\tau = 2b\text{VWC}$. ERA5-Land LAI provides a dynamic characterization of the vegetation, while the SMAP SCA-based VWC is derived from NDVI climatology (developed from ten years of MODIS data) [43]. Additionally, the use of VWC is recommended for low vegetated areas [39].

Consequently, the use of dynamic LAI information for the estimation of τ generates better sensitivity over the ABZ, which contains a large fraction of high vegetation areas, i.e., boreal forests.

The addition of the angular dependence of the signal propagation path through the vegetation cover in $\Gamma_{\text{model 4}}$ does not significantly improve the sensitivity with respect to $\Gamma_{\text{model 2–3}}$. On the other hand, the performance of $\Gamma_{\text{model 2–3}}$ is very similar. The accuracy and spatial resolution of the roughness parameter h used in $\Gamma_{\text{model 3}}$ should be improved to properly account for the small-scale surface roughness in the GNSS-R scenario. However, this is (to the authors' knowledge) the only source of auxiliary information available at a global scale. Consequently, for the following analysis, $\Gamma_{\text{model 2}}$ will be used for constructing $\Delta(t)$. The optimum value α_{opt} that improves the sensitivity is also derived for the different surface types under study, by empirically tuning the optimal operating point on the corresponding ROC curves (Fig. 2). This adjustment accounts for potential uncertainties in ERA5-Land data, the two-way attenuating path through the vegetation cover in the GNSS-R case, and potentially also for the effect of frozen vegetation, which modifies the attenuation of the vegetation layer [44]. Two sample cases are depicted for high vegetation and low vegetation (Fig. 2). For high vegetation, $\alpha_{\text{opt}} = 2$ [Fig. 2(a)]. Intermediate α values above or below α_{opt} are translated into lower sensitivity ROC curves. For low vegetation, the increment of sensitivity is significant from $\alpha \sim 0.5$ to $\alpha \sim 2.5$, and then, the improvement gradually saturates up to $\alpha_{\text{opt}} = 8.5$.

The optimized sensitivity of $\Delta(t)$, using $\Gamma_{\text{model 2}}$, to F/T surface changes is shown through the ROC curves corresponding to all the surface types (Fig. 3). The PD versus FAR relationship is encouraging even for areas with high small-scale surface roughness and high vegetation, i.e., the sensitivity of $\Delta(t)$ to F/T transitions enables accurate characterization of the soil surface state over the ABZ.

C. GNSS-R Surface Sampling

The spatiotemporal analysis is performed for one day, one week, ten days, and one month (Fig. 4) over a 0.1° $\times$ 0.1 grid [16], [17]. A temporal resolution of ten days ($\pm$5 days around a designated day) is selected for this study based on the number of observations per pixel (i.e., number of reflectivity Γ values available for averaging) [Fig. 4(a)–(d)]. This approach provides a reasonable tradeoff between spatial and temporal resolution. Future large GNSS-R SmallSat constellations could provide hourly or better temporal resolution without degraded spatial resolution. Alternatively, combining measurements by all the available GNSS-R constellations could enable to observe day and night F/T fluctuations, which are of special interest in Spring and Fall. To do so, intercalibration strategies and standardization methods would be required [45]. ERA5-Land and SMAP auxiliary products are converted to the new grid, determined by Spire.

D. Multithresholding Method

An optimized seasonal scale factor model $\Delta(t)$ was previously proposed. This scale factor is the foundational element for the F/T STA algorithm. The next step of the retrieval

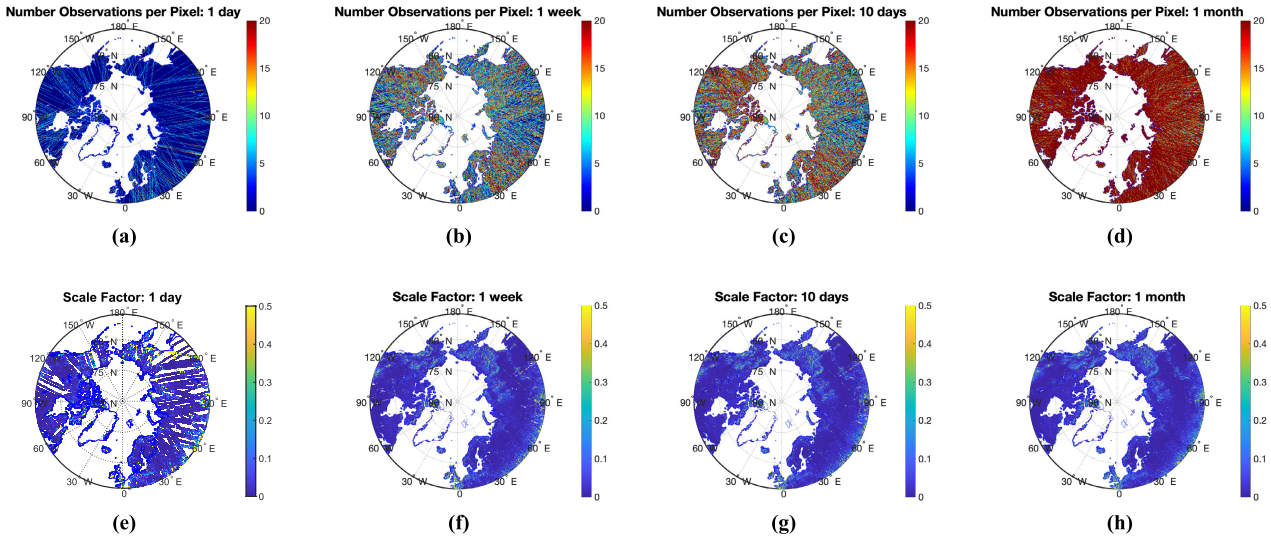


Fig. 4. Spatiotemporal analysis of the number of Spire GNSS-R observations (a)–(d) and (e)–(h) seasonal scale factor model $\Delta(t)$ (natural number) with $\Gamma_{\text{model 2}}$ for a 0.1° × 0.1° grid: (a) and (e) one day, (b) and (f) one week, (c) and (g) ten days, and (d) and (h) one month. Data correspond to January 2022. $\Delta(t)$ is very low (below the per-pixel freezing threshold) and homogenous over ABZ, which means that the surface is frozen. The larger the temporal window, the better the spatial coverage. Future larger constellations of GNSS-R SmallSats will enable to increase the spatial resolution of the grid cell by augmenting the number of observations.

algorithm is the definition and calculation of localized scale factor thresholds $\Delta_{\text{threshold}}$ at each pixel. At each pixel, if $\Delta(t)$ is below the corresponding $\Delta_{\text{threshold}}$, then the pixel is assumed to be frozen. Conversely, each surface pixel with $\Delta(t)$ above $\Delta_{\text{threshold}}$ is assumed to be thawed. The threshold at each pixel is determined by a linear fitting function of $\Delta(t)$ with $T_{\text{air}}(t)$ in the range $-10\ ^\circ\text{C} < T_{\text{air}} < 10\ ^\circ\text{C}$ using a multiyear time series (since 2021) generated every three days, with a temporal resolution of ten days. Estimating T_{soil} is more complicated than T_{air}, introducing higher uncertainties. T_{soil} by ERA5-Land is set at the middle of each layer (3.5 cm for layer 1), and heat transfer is calculated at the interfaces between them [32].

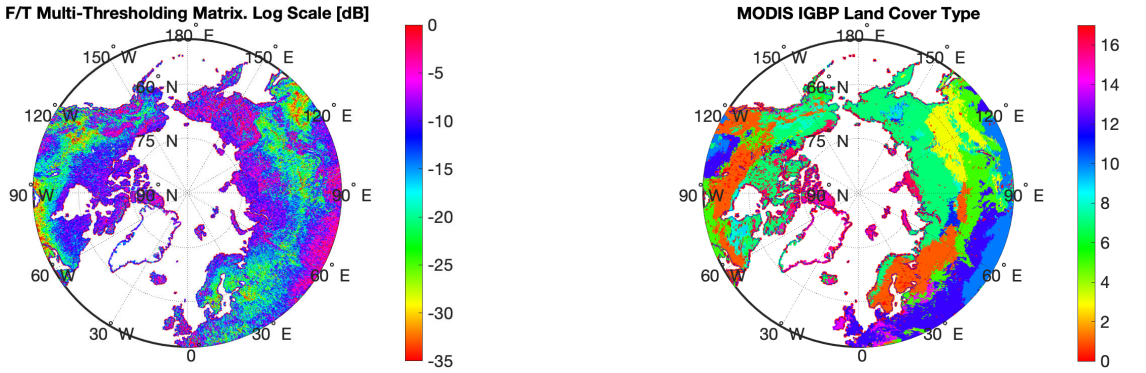
The threshold is derived from the fitting curves at $T_{\text{air}} = -3\ ^\circ\text{C}$. This threshold was empirically selected below 0 °C to mitigate potential errors in ERA5-Land reanalysis data, i.e., if T_{air} data predicted by ERA5-Land were higher than the actual air temperature. Additionally, this method accounts for the thermal inertia of the soil surface. In other words, the surface takes some time to become frozen when the air temperature decreases below 0 °C. The resulting F/T multithresholding matrix for all pixels is shown in logarithmic scale in Fig. 5(a). The dynamic range is significantly high, enabling a proper accounting for the impact of variations in land cover type, as illustrated by the IGBP MODIS land cover product [Fig. 5(b)].

The performance of the F/T STA algorithm is shown for one sample case at Krasnoyarsk Krai (latitude 76.2°N and longitude 103.6°E) (Fig. 6). The F/T classification can be seen to generally agree with the surface temperature T_{soil}, even under a thick layer of dry snow, because the signal penetration depth through snow is high at the L-band [46]. Scattering effects in the snowpack can be neglected at the L-band because the dominant size of ice structures is significantly smaller than the signal wavelength. However, F/T timing is challenging at the beginning of Fall, especially in Spring [47]. The presence of snow melt, temperature oscillations, and day and night F/T fluctuations all have an important influence. Fig. 6 illustrates this behavior in Spring.

The soil remains frozen, but the surface is misclassified as thawed due to the presence of melted snow, which increases Γ levels similarly as thawing soil. SMC fluctuations can also complicate F/T classification because the freezing of the soil water affects the soil permittivity in a roughly similar way as dry terrain. One example of the impact of SMC fluctuations on F/T determination is shown in Fig. 6. In Summer 2022, there is a marked drop in SMC caused by anomalously high T_{air}, which results in a falsely detected freeze state because dry soil permittivity reduces Γ. These isolated cases of false detection notwithstanding, a comprehensive examination of the number of false detection cases over the ABZ demonstrates an overall low rate of false detections and generally excellent performance of the F/T STA algorithm (Fig. 7). One land cover type, which appears to be particularly problematic, is grasslands (Fig. 7), which have a higher rate of false detections than other land cover types. False detections correspond to cases identified as frozen by the algorithm when $T_{\text{air}} > 5\ ^\circ\text{C}$. This approach accounts for potential situations when hypothetically the surface terrain could remain frozen because the snow cover isolates the soil from the atmosphere. For example, the surface could be frozen before snow starts covering the soil. Then, after the snowfall, the atmospheric temperature could increase, while the soil surface remained frozen because the snowpack acts as a thermal insulator [47]. Additionally, this mitigates potential errors in ERA5-Land reanalysis data (e.g., if T_{air} predicted by ERA5 was higher than the actual air temperature).

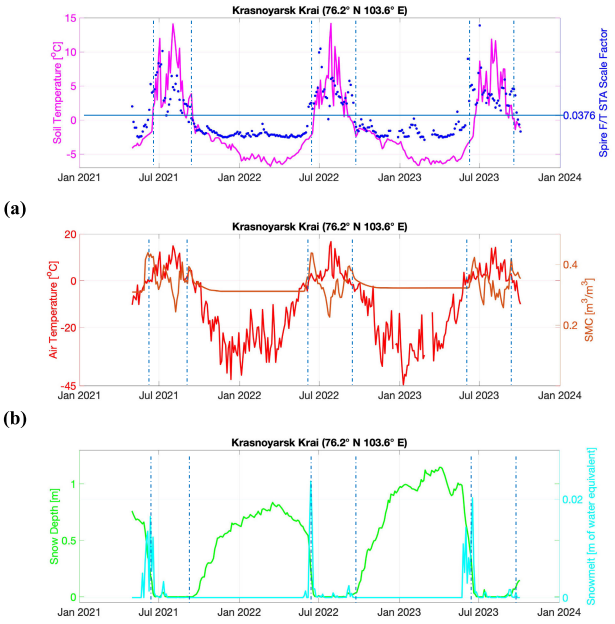
IV. Results

This section presents the main scientific findings within this investigation, including the corresponding discussions and the physical interpretation. This is structured in three different



(a) (b)

Fig. 5. (a) F/T multithresholding matrix in logarithmic scale. Each surface 0.1° × 0.1° grid cell with $\Delta(t)$ below the corresponding threshold is classified as frozen terrain. (b) IGBP MODIS land cover type: 0—Water Bodies, 1—Evergreen Needleleaf Forests, 2—Evergreen Broadleaf Forests, 3—Deciduous Needleleaf Forests, 4—Deciduous Broadleaf Forests, 5—Mixed Forests, 6—Closed Shrublands, 7—Open Shrublands, 8—Woody Savannas, 9—Savannas, 10—Grasslands, 11—Permanent Wetlands, 12—Croplands, 13—Urban and Built-Up, 14—Cropland/Natural Vegetation Mosaic, 15—Permanent Snow and Ice, 16—Barren or Sparsely Vegetated, and 17—Unclassified.



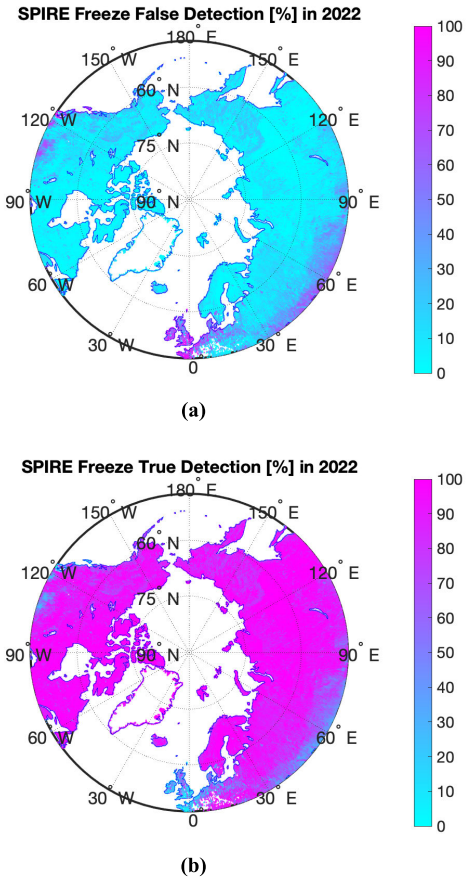
(a) (b) (c)

Fig. 6. Time series analysis at Krasnoyarsk Krai (IGBP Barren or Sparsely Vegetated) (latitude 76.2°N and longitude 103.6°E). (a) $\Delta(t)$ with $\Gamma_{\text{model 2}}$ versus T_{soil}. (b) SMC versus T_{air}. (c) M_{snow} versus D_{snow}. The time series are generated every three days, with a temporal resolution of ten days. The F/T classification generally agrees with T_{soil}, even under a thick layer of dry snow, because the signal penetration depth at L band is high. In mid-Summer, there is a drop in SMC caused by higher T_{air}, which is translated into a false detection case because dry soil permittivity reduces Γ.

subsections to show the results in a more clear and concise manner.

A. *Spire GNSS-R Versus SMAP Annual Frozen Soil Duration*

The annual frozen soil duration (days yr^{-1}) derived by the GNSS-R F/T STA algorithm is depicted in Fig. 8(a). The comparable frozen soil duration by the SMAP Enhanced L3 Radiometer Global and Northern Hemisphere Daily 9-km EASE-Grid F/T State, Version 3 data product [31] is also included [Fig. 8(b)]. The geophysical patterns show



(a) (b)

Fig. 7. Summary of Spire GNSS-R freeze detection statistics for all of 2022. (a) False detection (%). (b) True detection (%). 0.1° × 0.1 grid. Overall, these maps demonstrate the excellent performance of the F/T STA algorithm. The land cover type, which appears to be most problematic, is grasslands, i.e., IGBP land cover type 10 [Fig. 5(b)]. This region is quite dry, which complicates F/T classification because the freezing of the soil water affects the permittivity in a roughly similar way as dry terrain. False detections correspond to cases identified as frozen by the algorithm when ERA5-land $T_{\text{air}} > 5$ °C. This approach accounts for situations when the surface terrain could remain frozen because the snow cover isolates the soil from the atmosphere. For example, the surface could be frozen before snow starts covering the soil. Then, after the snowfall, the atmospheric temperature could potentially increase, but the soil surface could remain frozen because the snowpack acts as a thermal insulator [47].

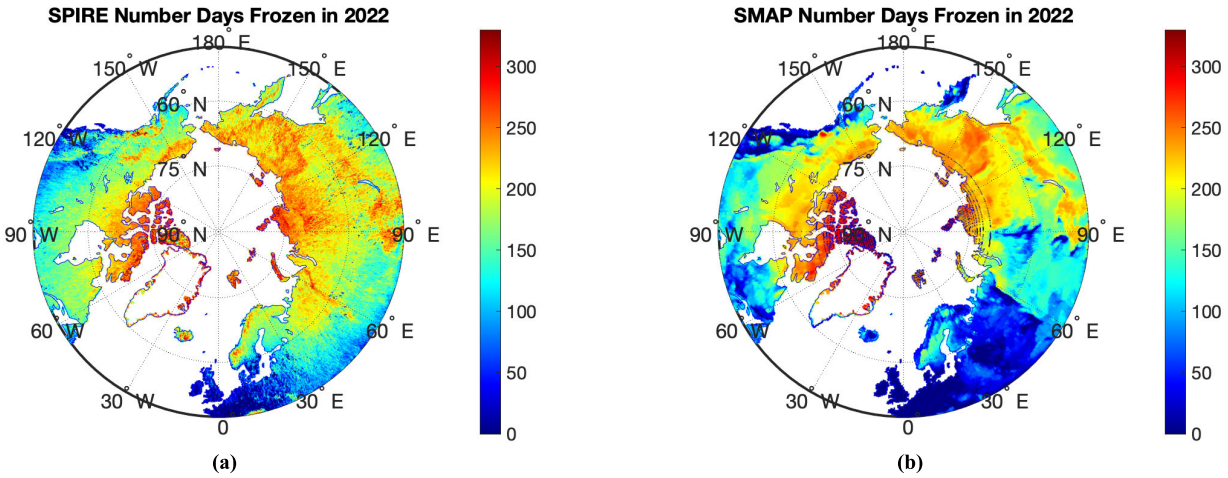


Fig. 8. Frozen soil duration (days yr^{-1}) retrieved by (a) Spire GNSS-R F/T STA algorithm and (b) SMAP Radiometer F/T Data Product L3_FT_P_E [31]. 0.1° × 0.1 grid. The SMAP "never frozen" and "never thawed" masks by 36.5-GHz AMSR-E and AMSR2 brightness temperature are probably affected by the snowpack. The Spire GNSS-R frozen soil duration map looks more similar to the frozen soil duration map in (Fig. 4, [48]).

similarities, e.g., in Siberia, Northern Canada, and Northern Alaska. Overall, the magnitude (days yr^{-1}) of the frozen soil duration in both maps is of the same order, where higher latitudes and elevations generally show higher frozen soil durations. On the other hand, some differences are identified in Europe (from the Ural Mountains to Great Britain), including Northern Scandinavian countries and Iceland. Differences are also identified in Quebec province and British Columbia in North America. The GNSS-R frozen soil duration map looks more similar to a state-of-the-art frozen soil duration map, which is computed using a multilayer convolutional neural network driven by Advanced Microwave Scanning Radiometer-2 (AMSR-2) and SMAP brightness temperature multifrequency (1.4, 18.7, and 36.5 GHz) records and trained on surface (∼0–5 cm depth) soil temperature F/T observations (Fig. 4, [48]). On the other hand, the official SMAP product [Fig. 8(b)] uses a false alarm mitigation strategy, which could explain the differences [31]. This will be further evaluated in Section IV-B.

B. Spire GNSS-R Versus SMAP F/T Detection: Annual Evolution Analysis With Snow Thickness and Temperature

Fig. 9 shows the annual evolution of the frozen surface detected by Spire, as a function of snow depth D_{snow} (color is ERA5-Land D_{snow} [m]). GNSS-R can determine the F/T soil surface state, even under thick dry snow cover. GNSS-R missions, e.g., Spire, provide high signal penetration depth in dry snow because of the use of GNSS L-band signals [49]. However, increasing levels of snowmelt reduces the signal penetration depth. It is also worth highlighting the fact that, in addition to the snowpack, boreal forests occupy a significant portion of the ABZ. GNSS-R penetration depth through vegetation has also been demonstrated to be high, enabling the detection of even small water bodies, e.g., [50], [51]. Consequently, F/T surface state classification under forest canopies appears to be a significant contribution of GNSS-R to microwave remote sensing. Spire observations will complement the abilities by SMAP to measure soil surface F/T under forest canopies in the ABZ [52].

Fig. 10 shows the temporal evolution of the SMAP Enhanced L3 Radiometer Global and Northern Hemisphere Daily 9-km EASE-Grid F/T State, Version 3 data product [31] during 2022. These maps represent the extension of frozen terrain as a function of T_{snow} (color is ERA5-Land T_{snow} [°C]). The SMAP product uses auxiliary information by AMSR-E and AMSR2 36.5 GHz brightness temperature as well as Goddard Earth Observing System Forward Processing (GEOS-FP) surface temperature [31] to generate "never frozen" and "never thawed" maps [53]. Additionally, if the SMAP brightness temperature at vertical V- or horizontal H-polarization is above 273 K, the surface is assumed thawed, independently of the retrieval algorithm [31]. This false alarm mitigation strategy could explain some of the differences seen with respect to the Spire frozen terrain maps (Fig. 9), as well as the roughly straight border along the Ural Mountains separating frozen and thawed terrain [Fig. 10(a) and (b)].

GNSS-R measurements depend only weakly on the physical temperature of the Earth's surface. Thus, the snow cover state could have a smaller impact on GNSS-R. Moreover, the "never frozen" and "never thawed" masks by 36.5-GHz AMSR-E and AMSR2 brightness temperature are probably affected by the snowpack. Additionally, the fact that Spire's Earth surface sampling is independent of local time enables to provide uniformly distributed GNSS-R local sampling times. This could provide a robust measure of the surface F/T state. Finally, it is worth noting the differences in the temporal resolution of SMAP and Spire observations. SMAP has a native temporal revisit of 2–3 days or better for polar regions (north of ∼45°N) and three days or better globally. On the other hand, the Spire F/T maps derived here have a temporal resolution of ten days. In the future, as more polar orbiting GNSS-R satellites become available, the GNSS-R revisit time should be improved significantly. In this study, in order to compare the two products, the SMAP F/T state at each pixel

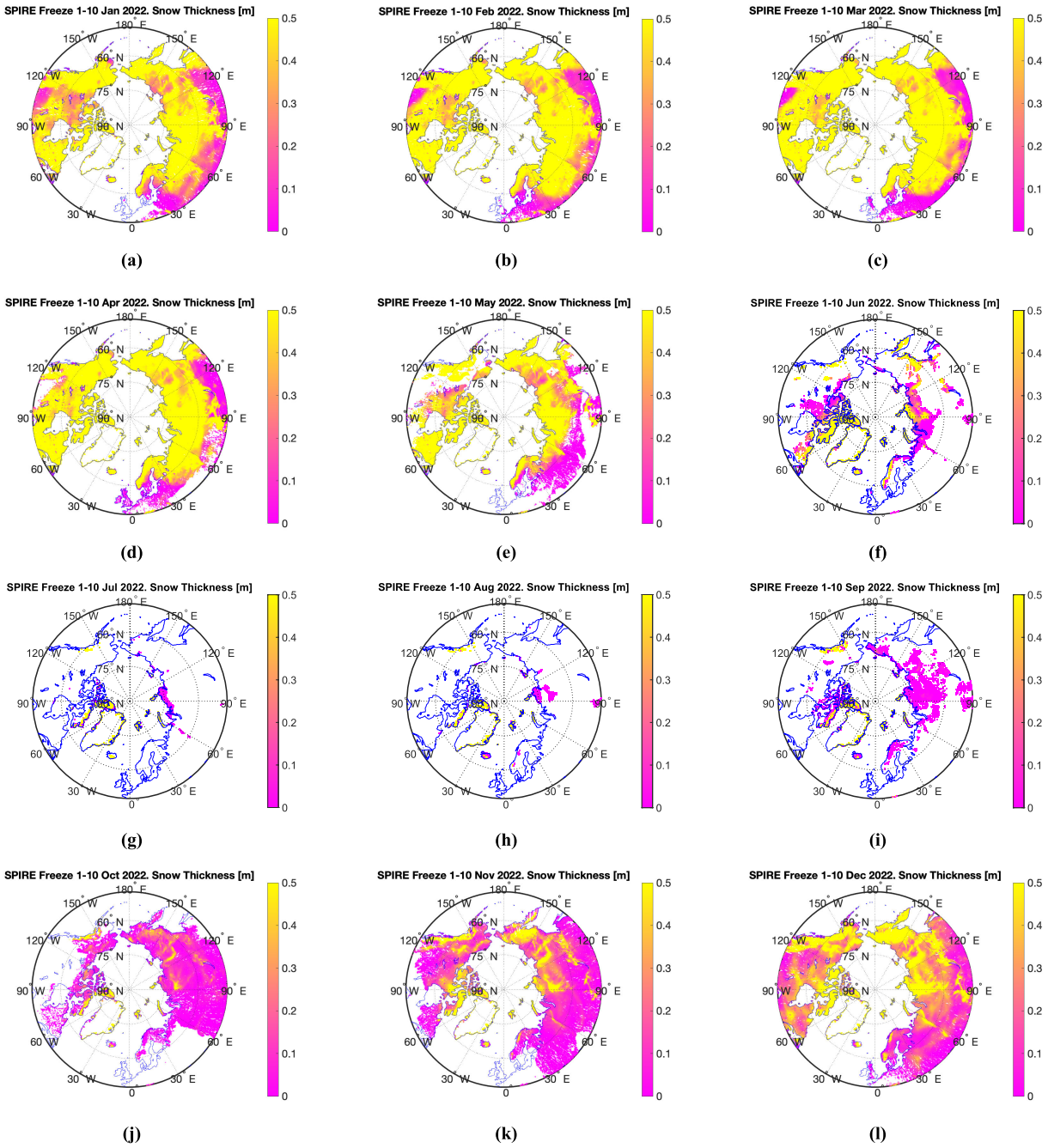


Fig. 9. Annual evolution of frozen terrain during 2022 by the Spire GNSS-R F/T STA algorithm. Color is ERA5-Land D_{snow} (m), i.e., all areas for which there is a color denote areas classified as frozen by Spire, and the color denotes the snow thickness in meters. Thus, white areas are not classified as frozen. 0.1° × 0.1 grid. Temporal resolution: ten days. The Spire GNSS-R L-band signal penetration depth is high over dry snow [46]. Spire GNSS-R F/T soil surface classification is feasible under a thick layer of snow $D_{\text{snow}} > 0.5$ m, even in boreal regions that are characterized by the presence of boreal forests.

is assumed to be frozen if it is frozen on any day within the ten-day period. Future dedicated studies at specific test sites would be required to more finely evaluate the differences and similarities of the two F/T products. The study presented here of Spire and SMAP annual trends provides a useful initial assessment of their comparison.

C. Spire GNSS-R Freeze Intensity

Traditional F/T microwave remote sensing products use a binary surface classification, i.e., a 100% frozen versus thawed surface state. A new F/T observable is defined here, which characterizes the intensity of the frozen state. This information is of interest to the climate modeling community [54].

The freeze intensity (FI) is defined as follows:

$$\text{FI} = 100\% \times \frac{\Delta_{\text{threshold}} - \Delta(t)}{\Delta_{\text{threshold}} - \Delta_{\text{min}}} \tag{7}$$

where Δ_{min} is the minimum value of $\Delta(t)$ and $\Delta_{\text{threshold}}$ is the F/T threshold value of $\Delta(t)$ [Fig. 5(a)]. FI is determined on a per-grid cell basis based on the dynamic range of the seasonal scale factor $\Delta(t)$ [Fig. 6(a)]. FI is 100% when $\Delta(t)$ is equal to its minimum value Δ_{min} in the time series (since 2021). From

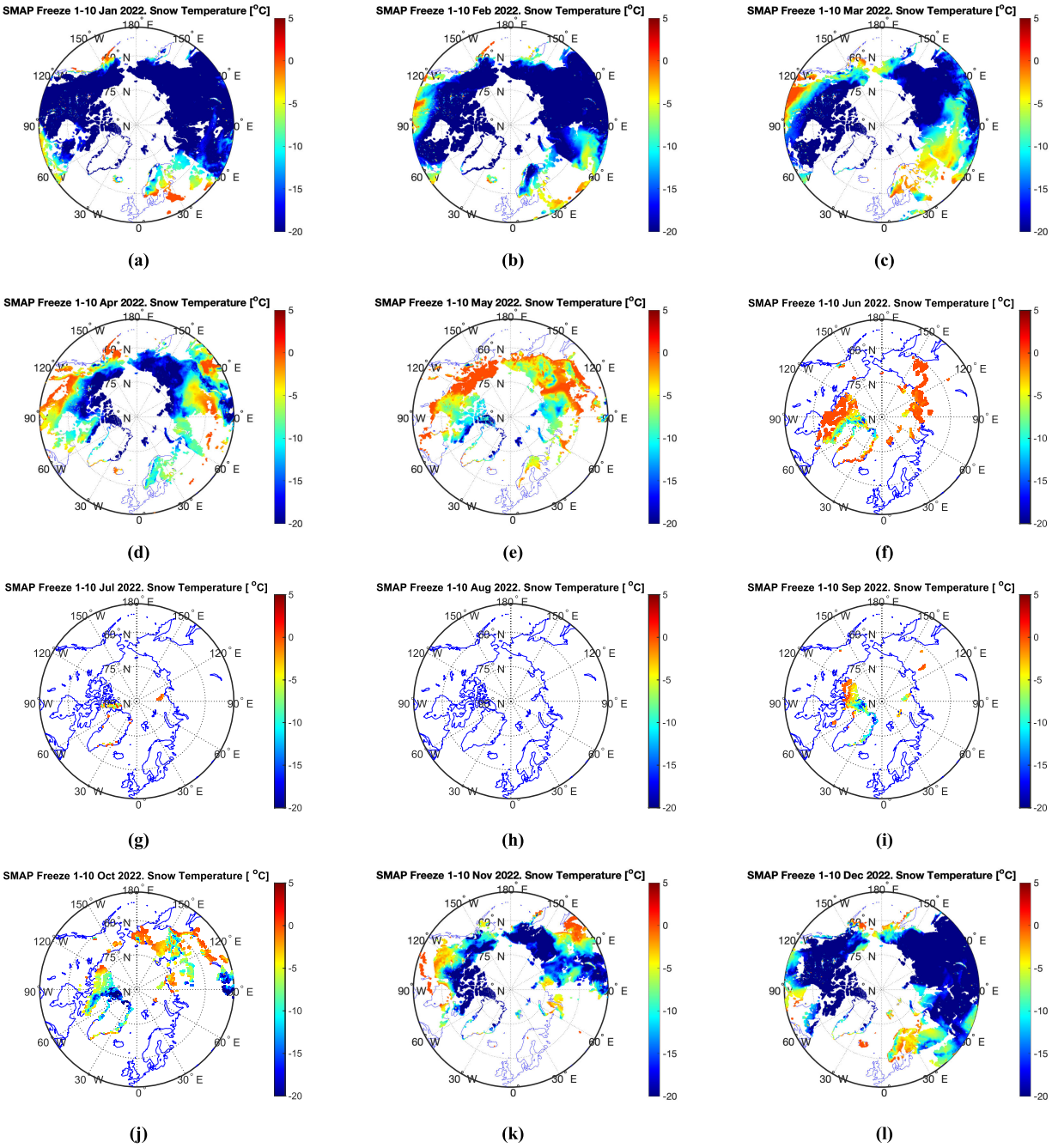


Fig. 10. Annual evolution of frozen terrain during 2022 by SMAP Enhanced L3 Radiometer Global and Northern Hemisphere Daily 9-km EASE-Grid F/T State, Version 3. Color is ERA5-Land T_{snow} (°C), i.e., all areas for which there is a color denote areas classified as frozen by SMAP, and the color denotes the snow temperature [°C]. Thus, white areas are not classified as frozen. 0.1° × 0.1 grid. Temporal resolution: ten days. The pixel is set to thaw when the SMAP brightness temperature is higher than 273 K. "Never frozen" and "never thawed" masks are applied. Masks are obtained from the AMSR-E and AMSR2 brightness temperature and the GEOS-FP surface temperature.

that value until the threshold $\Delta_{\text{threshold}}$, FI gradually decreases with increasing T_{air}, being 0% when $\Delta(t)$ is at the threshold $\Delta_{\text{threshold}}$. Fig. 11 (color is Spire GNSS-R FI [%]) shows the annual evolution of the frozen surface detected by Spire, as a function of this new observable. In Winter, FI is very high ∼100% (Fig. 11). There is a clear change in April/May when FI significantly decreases.

In Summer, most of the ABZ surface is thawed, except for limited areas at very high latitudes with persistent frozen terrain. In these areas, FI is found to be lower than ∼20%. In Fall, FI gradually increases, from September to December. For example, in the October map, almost all of Siberia is classified as frozen; however, FI is low-to-moderate. The physical interpretation is that only a portion of each grid cell is frozen, which reduces FI. Higher elevations, areas with dense vegetation, and valleys could remain frozen, while areas with more exposure to the solar radiation could be thawed. Additionally, day and night F/T fluctuations could have an impact on the magnitude of FI for a temporal window ∼10 days, especially at the transitions between freezing and thawing

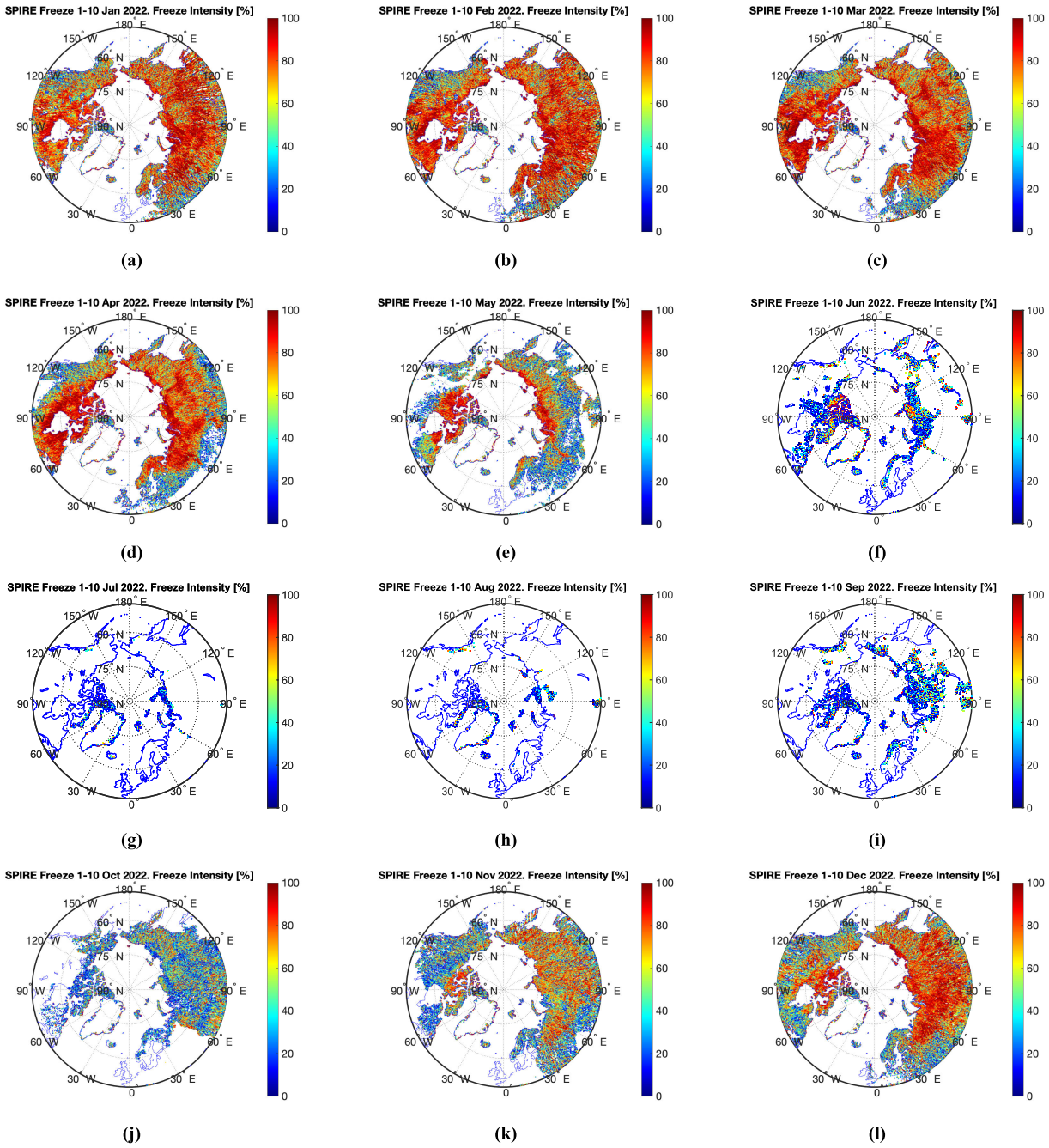


Fig. 11. Annual evolution of frozen terrain during 2022 by the Spire GNSS-R F/T STA algorithm. Color is Spire GNSS-R FI (%). White areas are not classified as frozen. 0.1° × 0.1 grid. Temporal resolution: ten days. FI is a percentual observable based on the dynamic range of the seasonal scale factor $\Delta(t)$. FI provides more complete information than classical binary F/T classifiers. FI represents a new type of freezing metric that could be of interest to the climate modeling community [54].

periods. Consequently, it can be said that this new observable FI provides a more complete and nuanced characterization of the surface state than classical binary F/T classifiers.

D. Spire GNSS-R Freezing and Thawing Periods

The F/T cycle changes the thermal–hydrological characteristics of soils. In high-altitude terrain and Northern regions, a large portion of the available water comes from snow. The soil is typically very wet at the beginning of Spring but dries out throughout the season because precipitation does not fully compensate for evapotranspiration. Additionally, if the soil surface is frozen, meltwater induced by snowmelt runs off and evaporates. Consequently, the aridity of the terrain increases, which complicates F/T classification. The freezing and thawing periods strongly determine the flow of soil water over the surface. Monitoring these periods is thus of significant importance to understand the effects of climate change in the ABZ. Fig. 6 shows how the moisture exchange is locked during the freezing periods, which are properly identified by the GNSS-R F/T STA algorithm. Warming temperatures due to climate change could significantly reduce the

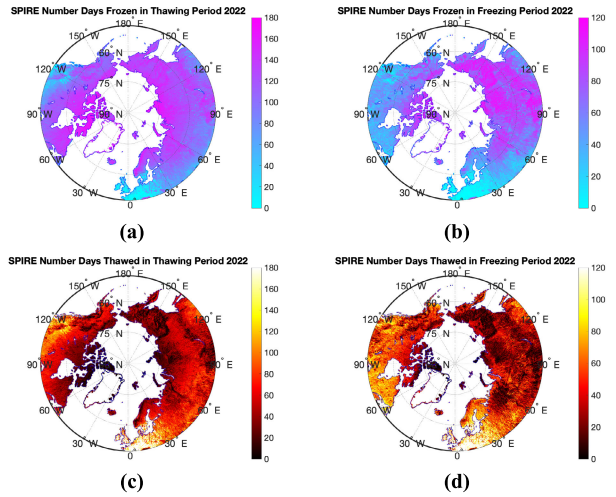


Fig. 12. Analysis of thawing (January–June) and freezing (September–December) periods. Number of days that the surface is frozen: (a) thawing period and (b) freezing period. Number of days that the surface is thawed: (c) thawing period and (d) freezing period. $0.1^\circ \times 0.1$ grid. Longer GNSS-R time series will enable to obtain the information on ABZ warming by analyzing the evolution of freezing and thawing periods. These periods determine when the moisture exchange with the atmosphere is locked.

duration of freezing periods, thus changing the hydrological condition in the ABZ. Longer GNSS-R time series in the ABZ would support further studies aimed at understanding these changes by interannual analysis of the freezing and thawing periods.

Remote sensing monitoring of these periods is complicated. The soil liquid water content does not freeze immediately when the snowfall begins to accumulate on the surface, and it can remain unfrozen for a long period of time or even never freeze below a snowpack, which is a strong thermal insulator [47]. On the other hand, Spring wet snow conditions additionally complicate the estimation of thawing soil. The GNSS-R ability to monitor these periods is demonstrated using Spire GNSS-R data for 2022. Fig. 12 shows the number of frozen [Fig. 12(a) and (b)] and thawed [Fig. 12(c) and (d)] days during the 2022 thawing [Fig. 12(a) and (c)] and freezing period [Fig. 12(b) and (d)] over the ABZ. The thawing period is January–June (Appendix) and the freezing period is September–December. Siberia, Scandinavia, Iceland, and Northern Canada show a higher number of frozen days during both, freezing and thawing periods. Additionally, it is observed that the number of thawed days during the thawing period is lower in high-altitude terrain, e.g., Norway and the Ural Mountains. On the other hand, the number of thawed days during freezing periods is more homogeneous. The physical interpretation is that high-altitude terrain could remain frozen longer into Summer.

V. Conclusion

A new F/T STA algorithm is developed over the ABZ using GNSS-R data by the NASA CSDA Spire SmallSat constellation. Five different semi-empirical reflectivity Γ models are proposed and evaluated for generating the seasonal scale factor $\Delta(t)$, which is the foundational element of the retrieval algorithm. This variety of Γ models is proposed to account for the GNSS signal attenuation through the vegetation cover and the impact of small-scale surface roughness over heterogeneous land cover types. A sensitivity study is performed using ROC curves to select the optimum model for F/T retrieval. It is found that $\Gamma_{\text{model 2}}$ provides the best PD versus FAR. This model dynamically estimates VOD as $\tau = \alpha \text{LAI}$, using auxiliary information by ERA5-Land, after empirically optimizing α for different values of VWC, h, and W_f. Then, a threshold $\Delta_{\text{threshold}}$ is determined at each surface pixel using a linear fitting function of $\Delta(t)$ with $T_{\text{air}}(t)$ in the range $-10\ ^\circ\text{C} < T_{\text{air}} < 10\ ^\circ\text{C}$. The threshold is obtained from the fitting curves at $T_{\text{air}} = -3\ ^\circ\text{C}$. The F/T retrieval algorithm is then applied, and a GNSS-R-based frozen soil duration map (days yr^{-1}) is obtained, comparing favorably with the SMAP enhanced radiometer F/T product. A new observable is also introduced, freeze intensity FI, which characterizes the degree of freezing more finely than a simple binary classifier. This determination of the freezing condition provides a more realistic product than classical binary F/T classifiers. FI informs on the spatiotemporal freezing heterogeneity of each pixel during the selected temporal window. Finally, the number of frozen and thawed days experienced during freezing and thawing transition periods is estimated over the ABZ. In conclusion, GNSS-R is shown to serve as a very effective F/T monitoring technique over the ABZ thanks to the signal penetration depth through dry snow and the vegetation canopy, e.g., boreal forests. However, increasing levels of snowmelt reduces the signal penetration depth, complicating soil surface F/T classification. Additionally, potential uncertainties in ERA5-Land should be evaluated in the future. Upcoming long-term GNSS-R time series over the ABZ can be expected to provide complementary information to other microwave remote sensing techniques, providing useful information about the impact of global warming on the water cycle in the ABZ.

Appendix
Thawing Evolution in May 2022

This section provides additional details about dynamic F/T monitoring by the Spire SmallSat constellation during an intense thawing event in May 2022. Fig. 13 shows the frozen surface detected by the Spire GNSS-R F/T STA algorithm, as a function of T_{snow}, every three days. These maps resolve dynamic changes in the extension of frozen terrain over ABZ, which gradually decreases from May to June. The changes show a time-variable geophysical pattern, where the highest latitudes (Arctic zone) and highest elevations (e.g., the Ural Mountain region) are associated with a generally larger frozen soil duration. Larger constellations of GNSS-R satellites are expected to generate data with an unprecedented spatiotemporal sampling resolution. This will enable to reduce the size of the grid cell size and increase the temporal resolution of F/T retrievals. The soil surface may be thawed during the day, but frozen during the night. Depending on the number of available GNSS-R satellites, the study of day and night F/T time series could further improve the accuracy of F/T timing information.

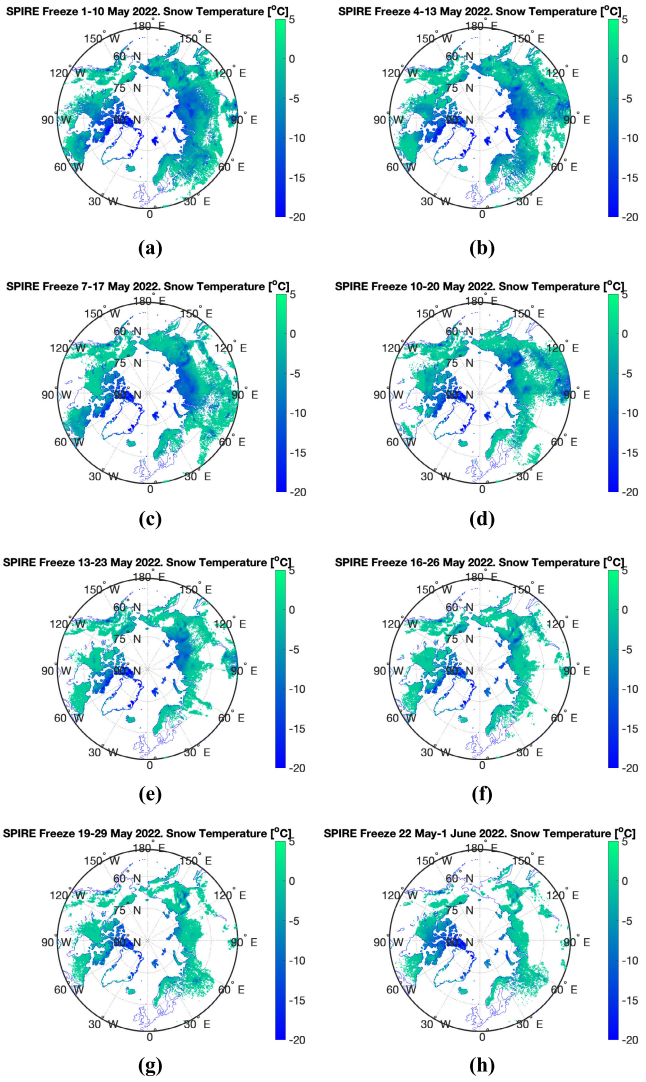


Fig. 13. Every three-day evolution of frozen surface extension by Spire GNSS-R F/T STA algorithm during an intense thawing event in May 2022. Color is ERA5-Land T_{snow} (°C). White areas are not classified as frozen. 0.1° × 0.1 grid.

ACKNOWLEDGMENT

This work utilized data made available through the NASA Commercial Smallsat Data Acquisition (CSDA) Program.

REFERENCES

[1] J. C. Comiso and D. K. Hall, "Climate trends in the Arctic as observed from space," *WIREs Climate Change*, vol. 5, no. 3, pp. 389–409, May 2014, doi: 10.1002/wcc.277.

[2] R. L. Thoman, T. A. Moon, and M. L. Druckenmiller, "Executive summary," NOAA, Washington, DC, USA, Tech. Rep., 2023, doi: 10.25923/5vfa-k694.

[3] T. A. Moon et al., "The expanding footprint of rapid Arctic change," *Earth's Future*, vol. 7, no. 3, pp. 212–218, Mar. 2019, doi: 10.1029/2018ef001088.

[4] K. Rautiainen et al., "SMOS prototype algorithm for detecting autumn soil freezing," *Remote Sens. Environ.*, vol. 180, pp. 346–360, Jul. 2016, doi: 10.1016/j.rse.2016.01.012. [Online]. Available: http://dx.doi.org/10.1016/j.rse.2016.01.012

[5] C. Derksen et al., "Retrieving landscape freeze/thaw state from soil moisture active passive (SMAP) radar and radiometer measurements," *Remote Sens. Environ.*, vol. 194, pp. 48–62, Jun. 2017, doi: 10.1016/j.rse.2017.03.007.

[6] J. Cohen, K. Rautiainen, J. Lemmetyinen, T. Smolander, J. Vehviläinen, and J. Pulliainen, "Sentinel-1 based soil freeze/thaw estimation in boreal forest environments," *Remote Sens. Environ.*, vol. 254, Mar. 2021, Art. no. 112267, doi: 10.1016/j.rse.2020.112267.

[7] J. Cohen et al., "Detection of soil and canopy freeze/thaw state in the boreal region with L and C band synthetic aperture radar," *Remote Sens. Environ.*, vol. 305, May 2024, Art. no. 114102, doi: 10.1016/j.rse.2024.114102.

[8] J. Chen et al., "Active layer freeze-thaw and water storage dynamics in permafrost environments inferred from InSAR," *Remote Sens. Environ.*, vol. 248, Oct. 2020, Art. no. 112007, doi: 10.1016/j.rse.2020.112007.

[9] M. Martín-Neira, "A passive reflectometry and interferometry system (PARIS): Application to ocean altimetry," *ESA J.*, vol. 17, no. 4, pp. 331–355, Dec. 1993.

[10] C. Ruf et al., "CYGNSS: Enabling the future of hurricane prediction [remote sensing satellites]," *IEEE Geosci. Remote Sens. Mag.*, vol. 1, no. 2, pp. 52–67, Jun. 2013, doi: 10.1109/MGRS.2013.2260911.

[11] M. J. Unwin et al., "An introduction to the HydroGNSS GNSS reflectometry remote sensing mission," *IEEE J. Sel. Topics Appl. Earth Observ. Remote Sens.*, vol. 14, pp. 6987–6999, 2021, doi: 10.1109/JSTARS.2021.3089550.

[12] C. Chew et al., "SMAP radar receiver measures land surface freeze/thaw state through capture of forward-scattered L-band signals," *Remote Sens. Environ.*, vol. 198, pp. 333–344, Sep. 2017, doi: 10.1016/j.rse.2017.06.020.

[13] D. Comite, L. Cenci, A. Colliander, and N. Pierdicca, "Monitoring freeze-thaw state by means of GNSS reflectometry: An analysis of TechDemoSat-1 data," *IEEE J. Sel. Topics Appl. Earth Observ. Remote Sens.*, vol. 13, pp. 2996–3005, 2020, doi: 10.1109/JSTARS.2020.2986859.

[14] K. Rautiainen, D. Comite, J. Cohen, E. Cardellach, M. Unwin, and N. Pierdicca, "Freeze–thaw detection over high-latitude regions by means of GNSS-R data," *IEEE Trans. Geosci. Remote Sens.*, vol. 60, 2022, Art. no. 4302713, doi: 10.1109/TGRS.2021.3125315.

[15] H. Carreno-Luengo and C. S. Ruf, "Retrieving freeze/thaw surface state from CYGNSS measurements," *IEEE Trans. Geosci. Remote Sens.*, vol. 60, 2022, Art. no. 4302313, doi: 10.1109/TGRS.2021.3120932.

[16] H. Carreno-Luengo and C. S. Ruf, "Mapping freezing and thawing surface state periods with the CYGNSS based F/T seasonal threshold algorithm," *IEEE J. Sel. Topics Appl. Earth Observ. Remote Sens.*, vol. 15, pp. 9943–9952, 2022, doi: 10.1109/JSTARS.2022.3216463.

[17] C. Ruf et al., *CYGNSS Handbook*. Ann Arbor, MI, USA: Univ. of Michigan Press, 2016.

[18] J.-C. Juang, S.-H. Ma, and C.-T. Lin, "Study of GNSS-R techniques for FORMOSAT mission," *IEEE J. Sel. Topics Appl. Earth Observ. Remote Sens.*, vol. 9, no. 10, pp. 4582–4592, Oct. 2016, doi: 10.1109/JSTARS.2016.2575069.

[19] Z. Guo et al., "Soil moisture retrieval using BuFeng-1 A/B based on land surface clustering algorithm," *IEEE J. Sel. Topics Appl. Earth Observ. Remote Sens.*, vol. 15, pp. 4680–4689, 2022, doi: 10.1109/JSTARS.2022.3179325.

[20] Y. Sun et al., "GNOS-II on Fengyun-3 satellite series: Exploration of multi-GNSS reflection signals for operational applications," *Remote Sens.*, vol. 15, no. 24, p. 5756, Dec. 2023, doi: 10.3390/rs15245756.

[21] E. Cardellach et al., "Precise GNSS-R altimetry with the ESA PRETTY CubeSat: Initial in-orbit results," presented at the IEEE Int. Geosci. Remote Sens. Symp. (IGARSS), Athens, Greece, Jul. 2024.

[22] *Spire Near-Nadir GNSS-R Level 1 Product Manual V1.6*, Spire Global Inc., Vienna, VA, USA, 2024.

[23] *Muon Space*. Accessed: Dec. 6, 2024. [Online]. Available: https://www.muonspace.com/

[24] *Tianmu-1*. Accessed: Dec. 6, 2024. [Online]. Available: https://space.skyrocket.de/doc_sdat/tianmu-1.htm

[25] M. Hallikainen, F. Ulaby, M. Dobson, M. El-rayes, and L.-K. Wu, "Microwave dielectric behavior of wet soil—Part 1: Empirical models and experimental observations," *IEEE Trans. Geosci. Remote Sens.*, vol. GRS-23, no. 1, pp. 25–34, Jan. 1985, doi: 10.1109/TGRS.1985.289497.

[26] M. Dobson, F. Ulaby, M. Hallikainen, and M. El-rayes, "Microwave dielectric behavior of wet soil—Part II: Dielectric mixing models," *IEEE Trans. Geosci. Remote Sens.*, vol. GRS-23, no. 1, pp. 35–46, Jan. 1985, doi: 10.1109/TGRS.1985.289498.

[27] L. Zhang, J. Shi, Z. Zhang, and K. Zhao, "The estimation of dielectric constant of frozen soil-water mixture at microwave bands," in *Proc. IEEE Int. Geosci. Remote Sens. Symp. (IGARSS)*, Jul. 2003, pp. 2903–2905, doi: 10.1109/IGARSS.2003.1294626.

[28] M. M. Al-Khaldi et al., "An analysis of a commercial GNSS-R soil moisture dataset," *IEEE J. Sel. Topics Appl. Earth Observ. Remote Sens.*, vol. 17, pp. 15480–15493, 2024, doi: 10.1109/JSTARS.2024.3449773.
[29] *NASA Commercial Smallsat Data Acquisition (CSDA) Program*. Accessed: Dec. 6, 2024. [Online]. Available: https://www.earthdata.nasa.gov/esds/csda
[30] P. O'Neill et al., "SMAP level 2 & 3 soil moisture (passive). Algorithm theoretical basis document (ATBD)," Jet Propuls. Lab., Pasadena, CA, USA, Tech. Rep. JPL D-66480, 2021.
[31] S. Dunbar, X. Xu, A. Colliander, C. Derksen, J. Kimball, and Y. Kim, "SMAP level 3 radiometer freeze/thaw data products (L3_FT_P and L3_FT_P_E), algorithm theoretical basis document (ATBD)," Tech. Rep., 2020.
[32] J. Munoz-Sabater et al., "ERA5-Land: A state-of-the-art global reanalysis dataset for land applications," *Earth Syst. Sci. Data*, vol. 13, no. 9, pp. 4349–4383, Sep. 2021, doi: 10.5194/essd-13-4349-2021.
[33] H. Carreno-Luengo, A. Camps, J. Querol, and G. Forte, "First results of a GNSS-R experiment from a stratospheric balloon over boreal forests," *IEEE Trans. Geosci. Remote Sens.*, vol. 54, no. 5, pp. 2652–2663, May 2016, doi: 10.1109/TGRS.2015.2504242.
[34] M. P. Clarizia, N. Pierdicca, F. Costantini, and N. Floury, "Analysis of CYGNSS data for soil moisture retrieval," *IEEE J. Sel. Topics Appl. Earth Observ. Remote Sens.*, vol. 12, no. 7, pp. 2227–2235, Jul. 2019, doi: 10.1109/JSTARS.2019.2895510.
[35] A. Camps et al., "Sensitivity of GNSS-R spaceborne observations to soil moisture and vegetation," *IEEE J. Sel. Topics Appl. Earth Observ. Remote Sens.*, vol. 9, no. 10, pp. 4730–4742, Oct. 2016, doi: 10.1109/JSTARS.2016.2588467.
[36] P. Pampaloni and S. Paloscia, "Microwave emission and plant water content: A comparison between field measurements and theory," *IEEE Trans. Geosci. Remote Sens.*, vol. GRS-24, no. 6, pp. 900–905, Nov. 1986, doi: 10.1109/TGRS.1986.289705.
[37] J.-P. Wigneron et al., "Modelling the passive microwave signature from land surfaces: A review of recent results and application to the L-band SMOS & SMAP soil moisture retrieval algorithms," *Remote Sens. Environ.*, vol. 192, pp. 238–262, Apr. 2017, doi: 10.1016/j.rse.2017.01.024.
[38] B. Li, S. P. Good, and D. R. Urycki, "The value of L-Band soil moisture and vegetation optical depth estimates in the prediction of vegetation phenology," *Remote Sens.*, vol. 13, no. 7, p. 1343, Apr. 2021, doi: 10.3390/rs13071343.
[39] Eur. Space Agency. (2019). *Algorithm Theoretical Basis Document (ATBD) for the SMOS Level 2 Soil Moisture Processor Development Continuation Project*. Accessed: Dec. 6, 2024. [Online]. Available: https://earth.esa.int/eogateway/documents/20142/37627/SMOS-L2-SM-ATBD.pdf
[40] Eur. Centre for Medium-Range Weather Forecasts. (2019). *IFS Documentation—Cy46r1 Operational Implementation. Part IV: Physical Processes*. Accessed: Dec. 6, 2024. [Online]. Available: https://www.ecmwf.int/en/elibrary/81141-ifs-documentation-cy46r1-part-iv-physical-processes
[41] S. Boussetta, G. Balsamo, A. Beljaars, T. Kral, and L. Jarlan, "Impact of a satellite-derived leaf area index monthly climatology in a global numerical weather prediction model," *Int. J. Remote Sens.*, vol. 34, nos. 9–10, pp. 3520–3542, May 2013, doi: 10.1080/01431161.2012.716543.
[42] Y. Knyazikhin et al. (1999). *MODIS Leaf Area Index (LAI) and Fraction of Photosynthetically Active Radiation Absorbed by Vegetation (FPAR) Product (MOD15), Algorithm Theoretical Basis Document*. Accessed: Dec. 6, 2024. [Online]. Available: https://modis.gsfc.nasa.gov/data/atbd/atbd_mod15.pdf
[43] N. N. Das et al., "The SMAP and Copernicus sentinel 1A/B microwave active-passive high resolution surface soil moisture product," *Remote Sens. Environ.*, vol. 233, Nov. 2019, Art. no. 111380, doi: 10.1016/j.rse.2019.111380.
[44] D. Kumawat, A. Ebtehaj, M. Schwank, X. Li, and J.-P. Wigneron, "Global estimates of L-band vegetation optical depth and soil permittivity of snow-covered boreal forests and permafrost landscape using SMAP satellite data," *Remote Sens. Environ.*, vol. 306, May 2024, Art. no. 114145, doi: 10.1016/j.rse.2024.114145.
[45] H. Carreno-Luengo et al., *IEEE Standard for Spaceborne Global Navigation Satellite System-Reflectometry (GNSS-R) Data and Metadata Content*, IEEE Standard 4003-2021, 2021, doi: 10.1109/IEEESTD.2021.9594781.
[46] F. T. Ulaby et al., *Microwave Radar and Radiometric Remote Sensing*. Ann Arbor, MI, USA: Univ. of Michigan Press, 2014.
[47] L. Gao, A. Ebtehaj, J. Cohen, and J.-P. Wigneron, "Variability and changes of unfrozen soils below snowpack," *Geophys. Res. Lett.*, vol. 49, no. 4, pp. 1–12, Feb. 2022, doi: 10.1029/2021gl095354.
[48] K. Donahue et al., "Deep learning estimation of northern Hemisphere soil freeze-thaw dynamics using satellite multi-frequency microwave brightness temperature observations," *Frontiers Big Data*, vol. 6, pp. 1–15, Nov. 2023, doi: 10.3389/fdata.2023.1243559.
[49] L. Steiner, M. Meindl, and A. Geiger, "Characteristics and limitations of GPS L1 observations from submerged antennas: Theoretical investigation in snow, ice, and freshwater and practical observations within a freshwater layer," *J. Geodesy*, vol. 93, no. 2, pp. 267–280, Feb. 2019, doi: 10.1007/s00190-018-1147-x.
[50] C. S. Ruf et al., "A new paradigm in Earth environmental monitoring with the CYGNSS small satellite constellation," *Sci. Rep.*, vol. 8, no. 1, pp. 1–13, Dec. 2018, doi: 10.1038/s41598-018-27127-4.
[51] H. Carreno-Luengo, C. S. Ruf, S. Gleason, and A. Russel, "Detection of inland water bodies under dense biomass by CYGNSS," *Remote Sens. Environ.*, vol. 301, Feb. 2024, Art. no. 113896, doi: 10.1016/j.rse.2023.113896.
[52] A. Colliander et al., "SMAP detects soil moisture under temperate forest canopies," *Geophys. Res. Lett.*, vol. 47, no. 19, pp. 1–10, Oct. 2020, doi: 10.1029/2020gl089697.
[53] Y. Kim, J. S. Kimball, K. Zhang, and K. C. McDonald, "Satellite detection of increasing northern Hemisphere non-frozen seasons from 1979 to 2008: Implications for regional vegetation growth," *Remote Sens. Environ.*, vol. 121, pp. 472–487, Jun. 2012, doi: 10.1016/j.rse.2012.02.014.
[54] H. Bergstedt et al., "Deriving a frozen area fraction from METOP ASCAT backscatter based on Sentinel-1," *IEEE Trans. Geosci. Remote Sens.*, vol. 58, no. 9, pp. 6008–6019, Sep. 2020, doi: 10.1109/TGRS.2020.2967364.



Hugo Carreno-Luengo (Senior Member, IEEE) received the Ingeniero Aeronáutico degree (Plan de Estudios 2000, "B.Sc.+M.Sc."), specialization in Spacecrafts, from the Escuela Técnica Superior de Ingenieros Aeronáuticos (ETSIA), the Universidad Politécnica de Madrid (UPM), Madrid, Spain, in 2010, and the Ph.D. degree (cum laude) from the Department of Signal Theory and Communications (TSC), the Universitat Politècnica de Catalunya (UPC), Barcelona, Spain, in 2016.

He was a Postdoc Fellow at the NASA Jet Propulsion Laboratory (JPL), JPL-CalTech, Pasadena, CA, USA; and with the CYGNSS Science Team under a Juan de la Cierva (JdC) contract, CTTC, UPC Campus, Barcelona, Spain. In 2020, he joined the NASA CYGNSS Mission Team, working directly with the PI, as an Assistant Research Scientist at the University of Michigan (U-of-M) College of Engineering, Ann Arbor, MI, USA, under a contract with the NASA Science Mission Directorate. He currently serves as an Associate Research Scientist. He is the PI of the NASA Research Opportunities in Space and Earth Science (ROSES) Freeze/thaw wildfires Risk prEdiction (FIRE) project. His research interests include GNSS-Reflectometry methods, applications, and technology.

Dr. Carreno-Luengo was the recipient of the U-of-M Research Faculty Recognition Award by the Office of the Vice-Provost for Research in 2024. He is a member of the American Geophysical Union (AGU). He serves on the Editorial Board of MDPI Remote Sensing, and he is an Associate Editor of IEEE TRANSACTIONS ON GEOSCIENCE AND REMOTE SENSING.



Christopher S. Ruf (Life Fellow, IEEE) received the B.A. degree in physics from the Reed College, Portland, OR, USA, in 1982, and the Ph.D. degree in electrical and computer engineering from the University of Massachusetts at Amherst, Amherst, MA, USA, in 1987.

He has worked previously with Intel Corporation, Aloha, OR, USA; Hughes Space and Communication, El Segundo, CA, USA; the NASA Jet Propulsion Laboratory, Pasadena, CA, USA; and Pennsylvania State University, University Park, PA, USA. He is the Frederick Bartman Collegiate Professor of Climate and Space Science and the Director of the University of Michigan Space Institute, Ann Arbor, MI, USA, and a Principal Investigator of the NASA CYGNSS Mission. His research interests include remote sensing technology, and methods and applications.

Prof. Ruf is a member of American Geophysical Union (AGU) and American Meteorological Society (AMS) and the Vice Chair of Commission F of the URSI. He is a former Editor-in-Chief of IEEE TRANSACTIONS ON GEOSCIENCE AND REMOTE SENSING and has served on the Editorial Board of *Radio Science*, *Journal of Atmospheric and Oceanic Technology*, and *Scientific Reports*.



Scott Gleason (Senior Member, IEEE) received the B.S. degree in electrical and computer engineering from the State University of New York at Buffalo, Buffalo, NY, USA, in 1991, the M.S. degree in engineering from Stanford University, Stanford, CA, USA, in 1999, and the Ph.D. degree in applied physics from the University of Surrey, Surrey, U.K., in 2007.

He is currently the President of Daaxa LLC consulting company, Boulder, CO, USA, specializing in GNSS instruments, calibration, and remote sensing applications. He is a Co-Investigator on the science team and Instrument Scientist for the NASA CYGNSS mission. He has worked in the areas of astronautics, remote sensing, and global navigation satellite systems for more than 30 years, including at NASAs Goddard Space Flight Center; Stanford's GPS Laboratory; Surrey Satellite Technology Ltd.; Concordia University, Montreal, QC, Canada; Southwest Research Institute; the University Corporation for Atmospheric Research; and the National Oceanography Centre, Southampton, U.K.



Anthony Russel received the B.S. degree in computer science engineering from Michigan State University, East Lansing, MI, USA, in 2014.

He is a member of the Engineering Staff at the Space Physics Research Laboratory, College of Engineering, University of Michigan, Ann Arbor, MI, USA. His primary engineering activities involve algorithm development and large-scale data processing as a member of the Science Operations Center for the CYGNSS mission.